



A highly active Pd clusters hosted by magnesium hydroxide nanosheets promoting hydrogen storage

Lixia Ge^{a,b}, Yanfeng Zhu^{a,b}, Minghuang Qiu^a, Shuai Yang^{c,d}, Nannan Sun^{a,*}, Wei Wei^{a,c}, Jiong Li^d, Xinqing Chen^{a,b,**}

^a CAS Key Laboratory of Low-carbon Conversion Science and Engineering, Shanghai Advanced Research Institute, Chinese Academy of Sciences, Shanghai 201210, China

^b University of Chinese Academy of Sciences, Beijing 100049, China

^c School of Physical Science and Technology, ShanghaiTech University, Shanghai 201210, China

^d Shanghai Synchrotron Radiation Facility, Zhangjiang National Lab, Shanghai Advanced Research Institute, Chinese Academy of Sciences, Shanghai 201210, China

ARTICLE INFO

Keywords:

Liquid organic hydrogen carrier
Dehydrogenation
Nanosheets
Heterogeneous catalyst
N-ethylcarbazole

ABSTRACT

Liquid organic hydrogen carriers (LOHCs) represent promising candidates for large-scale hydrogen storage, yet the design of high-efficiency and low-cost catalysts on the dehydrogenation of LOHCs remains challenging. Herein, we develop a two-dimensional (2D) magnesium hydroxide nanosheet that hosts Pd clusters (Pd/Mg(OH)₂) for the dehydrogenation of dodecahydro-N-ethylcarbazole (12H-NEC), an important reaction for H₂ transportation. The catalyst boosts the activity up to a 12H-NEC conversion of 100 % and the hydrogen release of 5.72 wt% with a low metal loading of 0.5 wt%, while the hydrogen release on Pd/MgO is only 2.34 wt% with the conversion rate of 71 % under the same conditions. Coupling various characterization technologies (HAADF-STEM, EXAFS, EPR and *In-situ* DRIFTS) with DFT calculations, it was found that the work function of magnesium hydroxide nanosheets for the dehydrogenation reaction due to the strong metal-support interaction, which makes Pd species have better dispersion, forms Pdⁿ⁺-OH stable Pd cluster and reduces the dehydrogenation barrier as well, thus enhancing the dehydrogenation performance and improving the hydrogen production greatly. This work provides a new promising way to design advanced dehydrogenation catalyst with high activity for the hydrogen storage.

1. Introduction

Nowadays, hydrogen is a promising source of energy featured by high-energy value, clean and renewable, and has attracted more and more attention in the world [1,2]. However, the rapid development and large-scale use of hydrogen energy is limited by the difficulties of hydrogen storage and transportation [3–5]. The methods of hydrogen storage mainly include physical hydrogen storage (compressed hydrogen, liquefied hydrogen and porous material) and chemical hydrogen storage (metal hydride, liquid organic hydrogen carriers) [2, 6]. Among them, liquid organic hydrogen carriers (LOHCs) show great advantages in hydrogen storage due to their high hydrogen storage capacity, mild reaction temperature, good reversibility, and can discharge high-purity H₂ directly used in fuel cells [7–10]. The realization of LOHCs hydrogen storage process is based on the catalytic conversion

between hydrogen rich and hydrogen poor organic compounds through reversible hydrogenation and dehydrogenation. Therefore, it is very important to design catalysts with high activity and selectivity for hydrogen storage.

Significantly, one series of LOHCs, such as N-ethylcarbazole/dodecahydro-N-ethylcarbazole (NEC/12H-NEC) [11,12], has attracted many researchers' attention due to its high hydrogen storage capacity (5.8 wt%), low dehydrogenation temperature (160–200 °C) and 99.99 % high-purity hydrogen generation. Previous reports indicated that the catalysts prepared by Pd [13–16] and Pt [17–20] metal supported on carbon, Al₂O₃ [21], SiO₂ [22], TiO₂ [23] shown excellent 12H-NEC dehydrogenation properties (Table S1). However, the precious metal loading of reported catalysts is normally kept at about 5 wt%. Some studies have shown that metal species are the main active components of LOHCs dehydrogenation [24–26]. Therefore, many researchers carried

* Corresponding author.

** Corresponding author at: CAS key Laboratory of Low-carbon Conversion Science and Engineering, Shanghai Advanced Research Institute, Chinese Academy of Sciences, Shanghai 201210, China.

E-mail addresses: sunnn@sari.ac.cn (N. Sun), chenxq@sari.ac.cn (X. Chen).

<https://doi.org/10.1016/j.apcatb.2023.122793>

Received 14 February 2023; Received in revised form 12 April 2023; Accepted 19 April 2023

Available online 20 April 2023

0926-3373/© 2023 Elsevier B.V. All rights reserved.

out a series of studies on the composition and state of metal species on supported catalysts [27,28]. For example, Cheng et al. explored the effect of different metals on the dehydrogenation performance of 12H-NEC and found that their initial catalytic activity for the dehydrogenation reaction was $\text{Pd} > \text{Pt} > \text{Ru} > \text{Rh}$ [29]. By quantifying the effects of various surface palladium species, Ma et al. found that fully exposed Pd clusters had high reactivity in the dehydrogenation reaction of 12H-NEC to NEC [30]. Besides, Fu et al. found that carbon-loaded PdO is more favorable for the dehydrogenation of dodecahydro-N-ethylcarbazole (12H-NEC) at lower temperatures, but requires higher Pd loading (5–10 wt%) [31,32]. It is still a big challenge for minimizing the amounts of noble metals until now.

In recent years, it has been found that the properties of catalyst supports, such as specific surface area, surface acidity, alkalinity or hydroxyl, have a greater impact on the dehydrogenation reaction [33]. Oh et al. found that the carbon content of the catalyst affects the physical and chemical properties of Al_2O_3 , which will indirectly affect the palladium particle size and metal dispersion, thus affecting the dehydrogenation performance of perhydro 2-(n-methylbenzyl)pyridine (12H-MBP) [34]. It has shown that the hydroxyl group of catalyst is not only beneficial for obtaining Pd nanoparticles with uniform and small particle size, but also stabilizes Pd^{n+} by forming $\text{Pd}^{n+}\text{-OH}$ bonds, thereby improving catalytic activity and selectivity [35]. Deng et al. prepared amorphous $\text{Bi}(\text{OH})_3$ -modified ultrathin Pd NSs by a one-step co-constrained growth method, and the catalyst showed stable EOR performance in the chrono current (CA) test [36]. Guo et al. developed single-atom Mo loaded on $\text{Co}(\text{OH})_2$ nanosheets for aerobic oxidative desulfurization reaction, which showed excellent low-temperature catalytic activity [37]. Besides, Tamao et al. demonstrated that supported palladium hydroxide catalysts were an efficient catalysts for synthesis of carbazoles and dibenzofurans [38]. Thus, these hydroxides showed great superiority in a lot of catalytic reactions. However, there have not been reported for the catalysts based on metal hydroxide supports for the dehydrogenation of LOHCs, which worth to be further investigated.

Herein, for the first time, we used two-dimensional (2D) magnesium hydroxide nanosheets, assembly of Pd species on them for the dehydrogenation of 12H-NEC. Compared with various characterization analysis, the structure-function relationship of $\text{Pd}/\text{Mg}(\text{OH})_2$ and Pd/MgO were studied, respectively. Meanwhile, the effect of magnesium hydroxide supported catalyst on dehydrogenation activity and the dehydrogenation mechanism of 12H-NEC were investigated by different characteristic technologies (HAADF-STEM, EXAFS, *In-situ* DRIFTS, EPR et al.) and DFT calculation. Our work demonstrates that the catalyst prepared by alkalinity support such as magnesium hydroxide nanosheet could be an effective strategy for dehydrogenation of nitrogen-containing aromatic hydrocarbons.

2. Experimental section

2.1. Synthesis of $\text{Mg}(\text{OH})_2$ nanosheets

Firstly, quickly added 100 mL of Na_2CO_3 aqueous solution (0.5 M) to 400 mL of $\text{Mg}(\text{NO}_3)_2$ aqueous solution (0.125 M) and stirred vigorously at room temperature. After 10 min, filtered and washed with deionized water, and then dried under reduced pressure to obtain MgCO_3 powder. The obtained MgCO_3 powder was transferred to a crucible and calcined at 500 °C in air atmosphere for 2 h. The heating rate shall be controlled at 2 °C min^{-1} . After cooling to room temperature, collected MgO for the next step. The hydrolysis of MgO was carried out at room temperature, and MgO was added to deionized water (1 mg/mL) with stirring. The dispersion gradually changed into colloidal suspension, showing obvious pearlescent effect, indicating the formation of flaky structure. After 1 h, the product was collected by filtration and dried under reduced pressure, and the obtained sample was named $\text{Mg}(\text{OH})_2\text{-NS}$.

2.2. Preparation of catalysts

The preparation of $\text{Pd}/\text{Mg}(\text{OH})_2$ catalysts as follows: A certain amount of Pd was loaded onto $\text{Mg}(\text{OH})_2\text{-NS}$ to prepare a dehydrogenation catalyst by incipient-wetness impregnation (IWI). Firstly, a certain amount of PdCl_2 solution (1 wt%) was added dropwise to 1 g $\text{Mg}(\text{OH})_2\text{-NS}$, stirred for 3 h at room temperature, and then evaporated in an 80 °C water bath. Finally, the sample was dried in a vacuum drying oven at 80 °C and named x %Pd/ $\text{Mg}(\text{OH})_2$.

The preparation of Pd/MgO catalyst as follows: A certain amount of $\text{Pd}/\text{Mg}(\text{OH})_2$ catalyst was transferred to a crucible and calcined at 400 °C for 6 h under an air atmosphere. The heating rate was controlled at 2 °C min^{-1} .

2.3. Catalyst characterizations

X-ray powder diffraction (XRD) patterns were obtained by the Rigaku Ultima IV X-ray diffractometer. The content of Pd in the catalyst was determined by an inductively coupled plasma atomic emission spectrometer (ICP-OES) with the instrument model Optima 8000, Perkin Elmer. N_2 physical adsorption was performed on the Quantachrome Autosorb-iQ2-MP nitrogen auto-sorption instrument at an adsorption temperature of −196 °C. The experiment of temperature-programmed desorption of carbon dioxide (CO_2 -TPD) was performed on a chemisorption instrument (Micromeritics ChemSorb 2920) connected to on-line mass spectrometry (MS, MKS Cirrus 2). The morphology and structure of the samples were tested by the ZEISS SUPRA55 SAPPHIRE Field emission scanning electron microscope (FE-SEM). The equipment accelerated voltage was 2.0 kV. TEM images were performed on a JEOL JEM-2011 instrument from JEOL Corporation at an accelerated voltage of 200 kV. The high angle annular dark-field scanning transmission electron microscopy (HAADF-STEM) was measured by JEOL ARM 300 F of JEOL company, and the acceleration voltage is generally 300 kV. *In-situ* diffuse reflectance spectroscopy of CO chemisorption (*In-situ* DRIFTS) is performed on a thermally sensitive FTIR spectrometer equipped with an MCT detector. The acquisition range is 4000–900 cm^{-1} , the resolution is 4 cm^{-1} , and the number of scans is 64 times. X-ray photoelectron spectroscopy (XPS) was performed under ultra-high vacuum conditions of 5×10^{-7} Pa, using the Thermo Scientific K-Alpha spectrometer with a source of Al K α (150 W, $h\nu=1486.6$ eV) to calibrate the test data with a C1s binding peak $E_b = 284.8$ eV. Electron paramagnetic resonance spectroscopy (EPR) experiments were performed on the Bruker A300 micro-spectrometer under the conditions of liquid nitrogen temperature (−196 °C), microwave frequency 9.85 GHz and microwave power of 20.36 mW. The X-ray Absorption Fine Structure (XAFS) is performed on the BL11B of the Shanghai Synchrotron Radiation Source (SSRF) with an operating voltage of 3.5 GeV and a maximum current of 240 mA in "charge" mode.

2.4. Catalytic tests

Hydrogen-rich LOHCs (12H-NEC, 12H-NPC or 8H-MID) were prepared according to our previous research [5], and the details are shown in the [supporting materials](#). The dehydrogenation experiments of hydrogen-rich LOHCs are as follows: 5 g of liquid hydrogen-rich LOHCs mixed with 0.5 g catalysts were added into a 100 mL stainless steel batch reactor (SLM microform, Beijing Century Senlong experimental apparatus Co., Ltd.). The autoclave was flushed with argon three times. Then, the reactor was heated to required temperature under magnetic stirring at 600 rpm at 101 kPa. After the reaction was finished and cooled naturally to room temperature. The collection product was dissolved in hot ethanol and filtered for analysis by GC and GC-MS.

2.5. DFT calculations

Spin-polarized DFT calculations were performed using the Vienna ab

initio simulation package (VASP) [39,40]. The generalized gradient approximation proposed by Perdew, Burke, and Ernzerhof (GGA-PBE) is selected for the exchange-correlation potential [41]. The pseudo-potential was described by the projector-augmented-wave (PAW) method [42]. The geometry optimization was performed until the Hellmann-Feynman force on each atom was smaller than $0.02 \text{ eV } \text{\AA}^{-1}$. The energy criterion was set to 10^{-6} eV in iterative solution of the Kohn-Sham equation.

3. Results and discussion

3.1. Structure characterization of catalysts

2D magnesium hydroxide nanosheets were synthesized by a two-step synthesis method. This process realized the conversion of MgCO_3 , MgO nanoparticles to Mg(OH)_2 nanosheets by controlling the reaction

kinetics [43,44], and the details are shown in the [supporting information](#) (Figs. S1-S2). The obtained Mg(OH)_2 samples exhibited an irregular petal-like distribution with a width of about 400 nm (Fig. 1b). Afterward the Pd species supported on magnesium hydroxide nanosheets were prepared by simply impregnating an appropriate amount of PdCl_2 solution (Fig. 1a), and the obtained samples were named as Pd/Mg(OH)_2 . As a comparison, Pd/MgO catalysts were prepared by calcining Pd/Mg(OH)_2 catalysts. After the loading of Pd nanoclusters on magnesium hydroxide, the morphology of catalysts did not change significantly (Fig. S3a). However, the morphology of the Pd/MgO catalysts are nanoparticles with a size of about 20–50 nm (Fig. S3b). Transmission electron microscope (TEM) image of Pd/Mg(OH)_2 and Pd/MgO catalyst were shown at Fig. S4, showing the Pd species are well dispersed on the external surface of Mg(OH)_2 nanosheets. However, Pd species are distributed on the surface of the Pd/MgO catalyst in the form of palladium nanoparticles ($\sim 2 \text{ nm}$). The atomic-scale structure of Pd/Mg(OH)_2

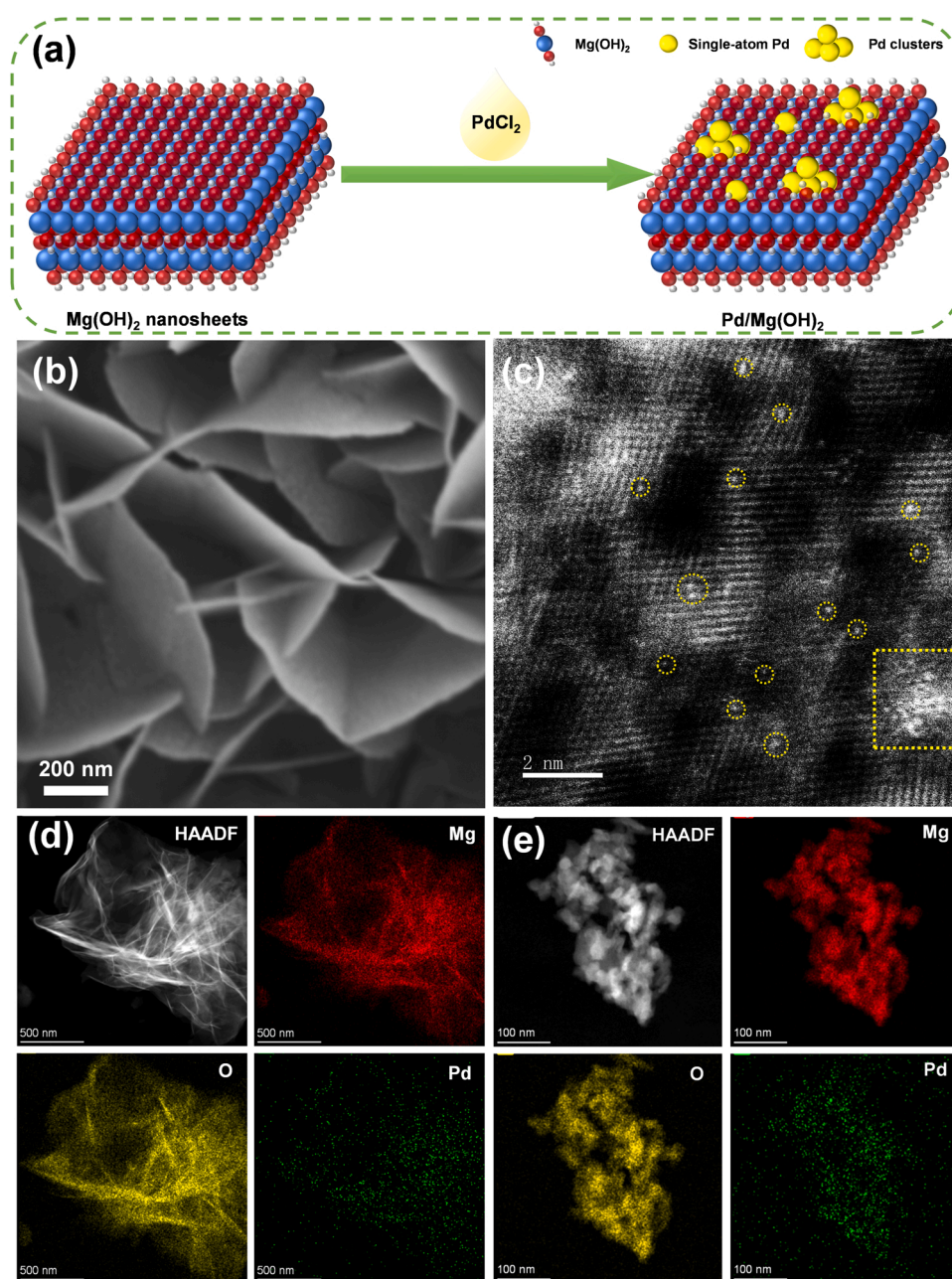


Fig. 1. Synthesis and characterizations of catalysts. (a) Schematic illustration of the preparation of Pd/Mg(OH)_2 . (b) FE-SEM image of Mg(OH)_2 nanosheets. (c) HAADF-STEM image of Pd/Mg(OH)_2 . EDS elemental mapping images for (d) Pd/Mg(OH)_2 and (e) Pd/MgO .

catalysts was displayed by high angle annular dark-field scanning transmission electron microscopy (HAADF-STEM). Fig. 1c show that both isolated single palladium atoms and palladium clusters (1–2 nm) all exist on the surface of $\text{Mg}(\text{OH})_2$ nanosheets, which are fully exposed Pd clusters. Furthermore, the elemental mappings for Mg, O and Pd elements of $\text{Pd}/\text{Mg}(\text{OH})_2$ and Pd/MgO catalysts are shown in Fig. 1d–e, S5. These results reveal that the Pd elements are uniformly distributed on the prepared samples.

The X-ray diffraction (XRD) patterns of different samples were shown in Fig. S6, the as-prepared $\text{Mg}(\text{OH})_2$, $\text{Pd}/\text{Mg}(\text{OH})_2$ samples all display typical diffraction peaks of the $\text{Mg}(\text{OH})_2$ with high crystallinity, the (101) diffraction peak at 37.98° is more intense compared with other peaks, which is consistent with the preferred orientation of $\text{Mg}(\text{OH})_2$ nanosheets shown by TEM results (Fig. S7). The diffraction peak of Pd/MgO sample is consistent with the characteristic peak of MgO . Besides, the characteristic peaks of PdO species cannot be detected in $\text{Pd}/\text{Mg}(\text{OH})_2$ and Pd/MgO samples due to the high dispersion and small metal loading. The FT-IR results of the samples showed that a strong absorption band was observed at 3699.8 cm^{-1} in $\text{Pd}/\text{Mg}(\text{OH})_2$ and $\text{Mg}(\text{OH})_2$ samples in Fig. S8 [45,46]. This absorption band comes from the tensile vibration of the hydroxyl group ($-\text{OH}$) on the surface of $\text{Mg}(\text{OH})_2$, which is not found in MgO . N_2 absorption/desorption isotherms (Fig. 2a, Table S2) show that the micropore specific surface area of $\text{Pd}/\text{Mg}(\text{OH})_2$ is slightly reduced compared with that of $\text{Mg}(\text{OH})_2$ support due to the occupation of partial pores by the Pd clusters. However, Pd/MgO catalyst display larger external specific surface area and more mesopore because of its nanoparticle properties as shown by SEM characterization. Inductively Coupled Plasma Optical Emission Spectrometer (ICP-OES) characterization shows that the Pd metal loading of the $\text{Pd}/\text{Mg}(\text{OH})_2$ and Pd/MgO catalysts is similar to the theoretical value, which is 0.53 % and 0.49 %, respectively (Table S2). In addition, carbon dioxide temperature-programmed desorption (CO_2 -TPD) measurements reveal the strength of surface basicity of $\text{Mg}(\text{OH})_2$, $\text{Pd}/\text{Mg}(\text{OH})_2$ and Pd/MgO catalysts (Fig. 2b). According to the CO_2 -TPD, the basicity of the

catalysts can be attributed to three different strengths, including weak basic sites ($27\text{--}147^\circ\text{C}$), medium basic sites ($147\text{--}377^\circ\text{C}$) and strong basic sites (above 377°C) [47,48]. All the samples indicate two characteristic peaks, corresponding to weak basic sites and medium basic sites, respectively. Differently, the two characteristic peaks of $\text{Pd}/\text{Mg}(\text{OH})_2$ shift to the low temperature region compared with $\text{Mg}(\text{OH})_2$. For Pd/MgO catalyst, it shows two relatively weak characteristic peaks at 84.9°C and 234.1°C respectively, which indicates that Pd/MgO catalyst has fewer basic sites. To verify the electronic properties of different catalysts, the EPR results of different catalysts are shown in Fig. 2c and S9. Only one Lorentz line was detected at a g value of 2.0034 for all samples in a magnetic field of 3460–3560 G. In addition, the EPR intensity of $\text{Pd}/\text{Mg}(\text{OH})_2$ and Pd/MgO catalysts is higher than that of $\text{Mg}(\text{OH})_2$ nanosheets, which indicates that the catalyst prepared by the Pd species supported on $\text{Mg}(\text{OH})_2$ nanosheets has a higher conduction band density than the catalyst prepared by MgO as a supporter, and involves a higher number of lone pairs of electrons [31]. The Pd 3d region for the $\text{Pd}/\text{Mg}(\text{OH})_2$ and Pd/MgO catalysts are indistinguishable due to the overlap of the Auger structure of Mg KLL with the Pd 3d region, and the binding energy of $\text{Pd } 3p_{1/2}$ is shown in Fig. S10. Compared with Pd/MgO catalyst, the $\text{Pd } 3p_{1/2}$ binding energy of $\text{Pd}/\text{Mg}(\text{OH})_2$ catalyst showed upfield shift of 0.6 eV, indicating that the electronic transfer and the strong interaction between Pd species and $\text{Mg}(\text{OH})_2$ support [47,49,50]. Then, we performed CO-adsorption diffuse reflectance infrared Fourier transform spectroscopy (CO-DRIFTS) measurements to clarify the dispersion of Pd species in different catalysts (Fig. 2d). The presence of FTIR bands on $\text{Mg}(\text{OH})_2$ supports indicates that the surface of $\text{Mg}(\text{OH})_2$ can adsorb CO molecules. The characteristic peak at $2000\text{--}2200\text{ cm}^{-1}$ and $1950\text{--}2000\text{ cm}^{-1}$ were attributed to the linear adsorption of CO molecules on Pd atomic sites and the bridge adsorption of CO molecules at Pd NPs sites, respectively [51]. The results show that both $\text{Pd}/\text{Mg}(\text{OH})_2$ and Pd/MgO samples contain two coexistence of Pd_1 and Pd NPs. However, more Pd species in $\text{Pd}/\text{Mg}(\text{OH})_2$ catalyst linearly adsorb CO molecules, indicating that Pd species in $\text{Pd}/\text{Mg}(\text{OH})_2$ have better

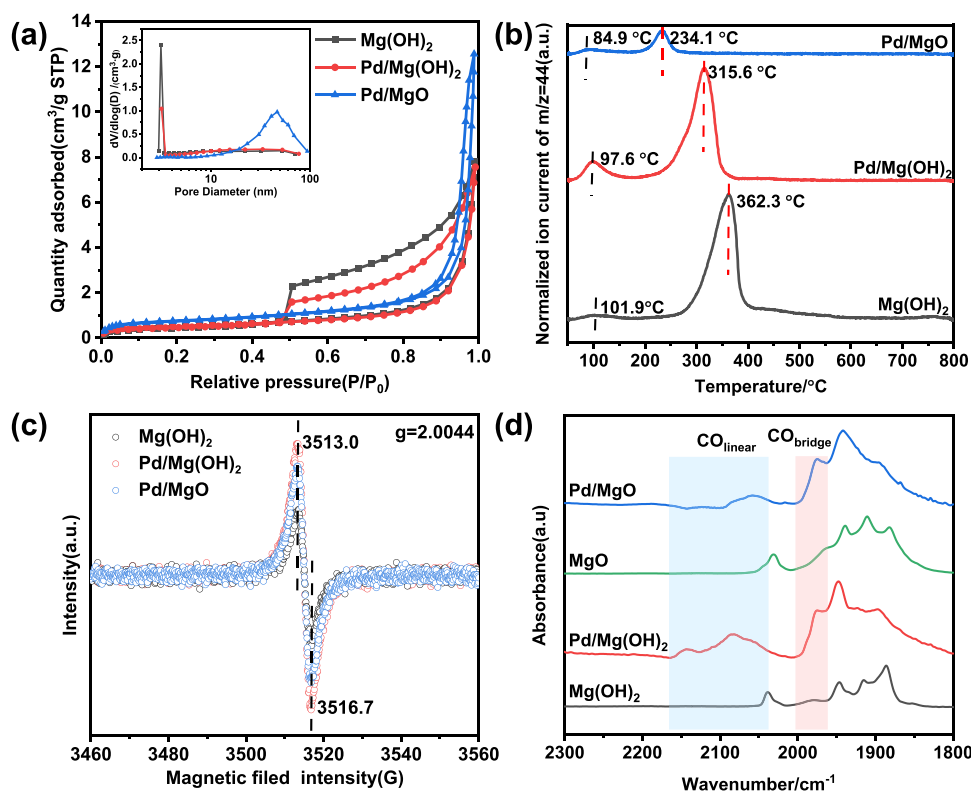


Fig. 2. Characterization of catalysts. (a) N_2 adsorption/desorption isotherms, (b) CO_2 -TPD profiles, (c) EPR patterns and (d) *In-situ* DRIFTS with CO adsorbed on $\text{Mg}(\text{OH})_2$, $\text{Pd}/\text{Mg}(\text{OH})_2$, MgO and Pd/MgO catalysts.

dispersion.

X-ray absorption fine structure (XAFS) measurements were performed to explore the chemical state and coordination environment of Pd metal species in the prepared samples. The X-ray absorption near edge structure (XANES) spectrum (Fig. 3a) shows that the valence of Pd/MgO and Pd/Mg(OH)₂ are between Pd foil and PdO, but close to the peak of PdO. It indicates that the chemical state of Pd species in both samples are in the oxidation state, which is consistent with the XPS results [52]. However, the energy of Pd/Mg(OH)₂ is slightly higher than that of Pd/MgO catalyst, which indicates that the chemical valence of Pd species in Pd/Mg(OH)₂ is higher. FT-EXAFS analysis was further carried out to analyze the coordination environment of Pd species in Pd foil, PdO, and Pd/MgO and Pd/Mg(OH)₂ samples. The results are shown in Fig. 3b-c, S11–12 and Table 1. For Pd/Mg(OH)₂ sample, it has an obvious peak (1.56 Å) and a relatively weak peak (2.91 Å), which comes from the contribution of Pd-O and Pd-Pd, respectively. Similarly, the Pd/MgO catalyst has an obvious peak (1.38 Å) and a relatively weak

peak (2.36 Å), which comes from the contributions of Pd-O and Pd-Pd, respectively. The EXAFS fitting results of Pd/Mg(OH)₂ catalyst show that the average coordination number and bond length of Pd-O are 3.1 ± 0.2 and 2.04 ± 0.01 Å, respectively, and that of Pd-Pd are 3.3 ± 0.3 and 2.75 ± 0.02 Å, respectively. The fitting results of Pd/MgO catalyst show that the average coordination number of Pd-O is 4.4 ± 0.2 and the average bond length is 2.04 ± 0.01 Å. The average coordination number of Pd-Pd is 8.4 ± 1.6 and the average bond length is 2.52 ± 0.02 Å. Compared with the Pd foil with more metal Pd-Pd coordination, the relatively low Pd-Pd coordination number indicates the existence of ultra-small Pd clusters in Pd/Mg(OH)₂ catalyst [53,54]. Compared with Pd/MgO catalyst, the lower coordination number and larger bond length of Pd/Mg(OH)₂ catalyst indicate that the Pd species in the catalyst has better dispersion. Wavelet transform extended X-ray absorption fine structure (WT-EXAFS) is used to analyze and investigate the dispersion of palladium species (Fig. 3d-g). The Pd/Mg(OH)₂ sample exhibits a characteristic peak of maximum intensity at 4.5 Å^{-1} , which can be

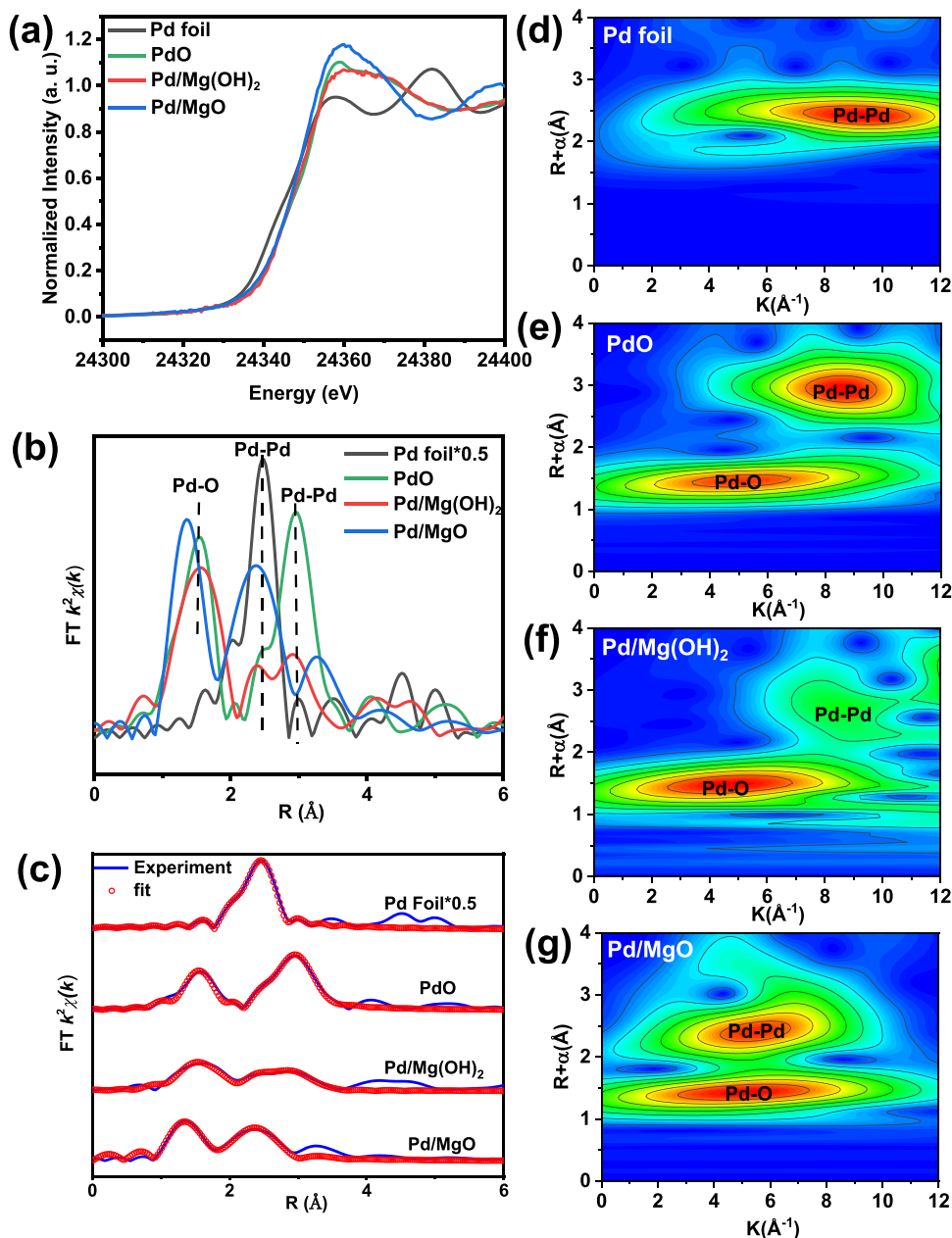


Fig. 3. (a) Pd K-edge XANES spectra, (b) FT k^3 -weighted Pd K-edge EXAFS spectra and (c) EXAFS fitting curve of Pd foil, PdO, and Pd/Mg(OH)₂. (d-g) Wavelet transform of Pd foil, PdO, Pd/Mg(OH)₂ and Pd/MgO.

Table 1
EXAFS fitting parameters at the Pd K-edge for various samples ($S_0^2 = 0.81$).

Samples	Shell	^a CN	^b R (Å)	^c σ^2	^d ΔE_0	^e R factor
Pd foil	Pd-Pd	12	2.74 ± 0.01	0.0055 ± 0.4	-5.0 ± 0.4	0.0026
PdO	Pd-O	4	2.03 ± 0.01	0.0022 ± 1.6	-0.4 ± 1.6	0.0095
	Pd-Pd	4	3.03 ± 0.01	0.0068 ± 2.5	-6.1 ± 2.5	
	Pd-Pd	8	3.40 ± 0.01	0.0052 ± 1.5	-8.0 ± 1.5	
Pd/Mg(OH) ₂	Pd-O	3.1 ± 0.2	2.04 ± 0.01	0.0082 ± 2.2	0.5 ± 2.2	0.0130
	Pd-Pd	3.3 ± 0.3	2.75 ± 0.02	0.0108 ± 1.5	10 ± 3.1	
	Pd-O	4.4 ± 0.8	2.04 ± 0.01	0.0026 ± 1.5	0.1 ± 1.5	
Pd/MgO	Pd-Pd	8.4 ± 1.6	2.52 ± 0.01	0.0070 ± 1.1	-3.3 ± 1.1	0.006
	Pd-O					

^a CN: coordination numbers

^b R: bond distance

^c σ^2 : Debye-Waller factors

^d ΔE_0 : the inner potential correction

^e R factor: goodness of fit

attributed to the coordination structure of Pd-O. In addition, there is a weak characteristic peak at 8.3 \AA^{-1} , which is attributed to the contribution of Pd-Pd. Similarly, the Pd/MgO catalyst also shows a characteristic peak of maximum intensity at 4.5 \AA^{-1} , which can be attributed to the coordination structure of Pd-O. There is also a strong characteristic peak at 5.62 \AA^{-1} , which may be attributed to the contribution of Pd-Pd or Pd-Mg. All in all, XAFS data show that there may exist single dispersed palladium atoms and completely exposed ultra-small clusters on Pd/Mg(OH)₂ sample [52].

3.2. Catalytic performance

We explored the catalytic dehydrogenation performance on different samples using perhydro-N-ethylcarbazole (12H-NEC) as a model compound (Fig. 4). The main intermediate products in the dehydrogenation process of 12H-NEC are octahydro-N-ethylcarbazole (8H-NEC) and tetrahydro-N-ethylcarbazole (4H-NEC) detected by GC and GC-MS, which is the same as reported in the Ref. [5]. Fig. 4a shows that Pd/Mg(OH)₂ exhibits the excellent catalytic performance, achieving complete conversion (100 %) of 12H-NEC and hydrogen release of 5.72 wt% with Pd loading of 0.5 wt%. It is noted that the maximum hydrogen release for the 12H-NEC/NEC system is 5.8 wt% calculated based on the substrate. Parent Mg(OH)₂ nanosheets has no catalytic

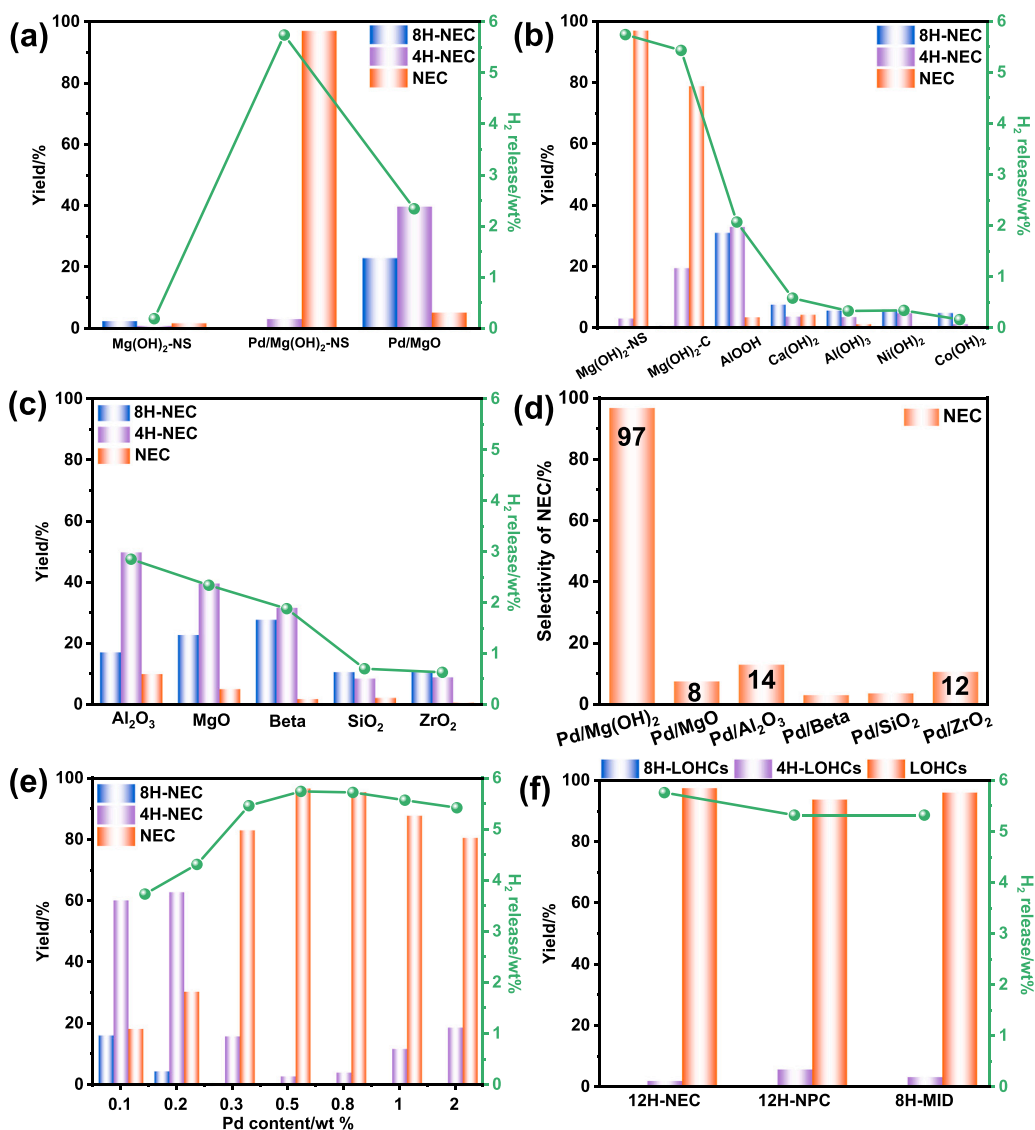


Fig. 4. Catalytic dehydrogenation performance of 12H-NEC over (a) Mg(OH)₂ nanosheets, Pd/Mg(OH)₂ and Pd/MgO, (b) Pd-based catalyst supported on hydroxide, (c) Pd-based catalyst supported on oxide. (d) Selectivity of NEC on Pd-based catalyst for the dehydrogenation of 12H-NEC. (e) Catalytic dehydrogenation performance of 12H-NEC over Pd/Mg(OH)₂ under different Pd content. (f) The dehydrogenation performance of HR-LOHCs over Pd/Mg(OH)₂. Reaction conditions: 5 g of 12H-NEC, 0.5 g of catalyst, 180 °C of reaction temperature, and 6 h of reaction time.

activity, suggesting that Pd species are active centers for catalytic dehydrogenation of 12H-NEC. In contrast, the catalytic activity of Pd/MgO catalysts decreased significantly, the conversion and hydrogen release rate of 12H-NEC over Pd/MgO are only 70.84 % and 2.34 wt% respectively, which indicates the interaction between the support and the active Pd clusters may play an important role in determining catalytic ability. Among all the investigated Pd-based catalyst supported on hydroxide (Fig. 4b), Pd/Mg(OH)₂ also exhibits superior catalytic dehydrogenation performance compared to other hydroxide supports, such as Co(OH)₂, Ni(OH)₂ and so on. A quantitative comparison of Pd-based catalyst supported on different oxides were studied in Fig. 4c, showing the hydrogen release rate is lower than 3.0 wt% on the Al₂O₃, MgO, ZrO₂ and so on. Since the 4H-NEC to NEC is the most difficulty step, the complete dehydrogenation product (NEC) selectivity of different samples were furthermore investigated in Fig. 4d, Pd/Mg(OH)₂ shows much higher selectivity for NEC (97.12 %), the selectivity of NEC on Pd/MgO is only 7.65 %, and the other Pd-based catalysts with the selectivity of NEC (<15 %). Based on the above catalytic results, we speculate that Mg(OH)₂ support with more basicity sites and two-dimensional nano-sheet structure can greatly promote the dispersion and catalytic activity of Pd metal [55]. The loading amount of Pd to Mg(OH)₂ nanosheets was optimized to 0.5 wt% in Fig. 4e, showing the catalytic performance increased with Pd loading when the loading below 0.5 wt%, and then slowly decreased at higher Pd loading. And 0.5 %Pd/Mg(OH)₂ exhibited excellent catalytic activity even at 160 °C, and the conversion rate of 12H-NEC can almost reach 100 % (Fig. S13). However, it is difficult to realize the complete conversion from 4H-NEC to NEC at 160 °C. In addition, Fig. S14 describes that the ratio of catalyst to reactant at 1/10 has better catalytic performance.

Furthermore, the cycle stability and reversible capacity was taken into consideration. The stability of Pd/Mg(OH)₂ was carried out for three times on the 12H-NEC dehydrogenation reactions at 180 °C for 6 h (Fig. S15). The conversion of the 12H-NEC maintained at 100 %, and the hydrogen release only decreased from 5.72 wt% to 5.56 wt%, 5.55 wt%. The characterizations of Pd/Mg(OH)₂ catalyst before and after the catalytic dehydrogenation reaction showed that there is no obvious change in the crystallinity and shape and size of Pd/Mg(OH)₂ and Pd/Mg(OH)₂-spent, and the basicity of the catalyst decreased slightly after repeated use (Figs. S16-18). This experimental result indicates that Pd/Mg(OH)₂ can remain stability and high activity after several cycles of dehydrogenation reaction. To test the generality of Pd/Mg(OH)₂ catalyst, we used other hydrogen-rich liquid organic hydrogen carriers (HR-LOHCs) as reactants for dehydrogenation reaction (Fig. 4f), such as octahydro-N-propylcarbazole (12H-NPC) and octahydro-2-methylindole (8H-MID). The experimental results showed that the conversion of 12H-NPC was as high as 100 %, and the hydrogen release was 5.23 wt% at 180 °C for 6 h. In addition, Pd/Mg(OH)₂ also exhibited high catalytic activity for 8H-MID, with a conversion rate of 94.03 % and a hydrogen release of 5.32 wt%. In a word, Pd/Mg(OH)₂ has excellent performance for the dehydrogenation of different LOHCs.

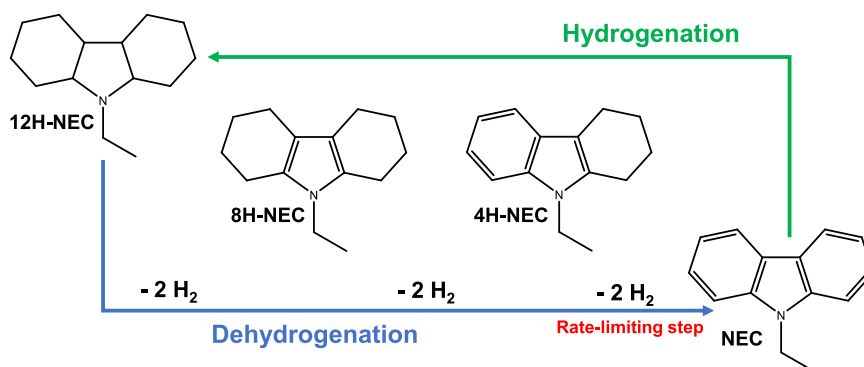
3.3. Mechanism investigation of the dehydrogenation of 12H-NEC

Previous studies have clarified that the main dehydrogenation process of 12H-NEC is shown in Scheme 1 [30]. Next, we explored and analyzed the curves of all species in the dehydrogenation of 12H-NEC over Pd/Mg(OH)₂ and Pd/MgO catalysts Fig. 5a-b, S19. The results indicated that 12H-NEC can be consumed to 8H-NEC quickly. Then 8H-NEC was converted to 4H-NEC as soon as produced from 12H-NEC. However, the conversion of 4H-NEC is the slowest, which indicates that the dehydrogenation of 4H-NEC to NEC is the rate-limiting step of the entire reaction. Compared with Pd/MgO catalyst, Pd/Mg(OH)₂ shows enhanced catalytic activity. The conversion rate of 12H-NEC reached 93.71 %, and the yield of 4H-NEC reached the summit within one hour. Afterwards, the dehydrogenation of 4H-NEC to NEC is carried out, and the process is basically completed at 300 min, with 12H-NEC conversion rate of 100 % and hydrogen release of 5.72 wt%. Differently, Pd/MgO catalyst showed lower catalytic activity for dehydrogenation of 12H-NEC, and the conversion of 12H-NEC was only 69.43 % and the main product is 4H-NEC, resulting the hydrogen release rate was only 2.53 wt% at 480 min

In order to further investigated the dehydrogenation mechanism of 12H-NEC, we studied the catalytic performance of different Pd metal sites, and found that Pd(OH)₂ show good catalytic activity in the absence of supporter (Fig. 5c). Besides, the catalytic dehydrogenation activity of 12H-NEC of catalysts prepared by different Pd metal species supported on the Al₂O₃ also showed great differences, namely Pd/Al₂O₃ < PdO/Al₂O₃ < Pd(OH)₂/Al₂O₃, indicating that Pd(OH)₂ is very beneficial to dehydrogenation of 12H-NEC. Several catalysts were prepared by deposition-precipitation of PdCl₂ on different supporters, using KOH as precipitators (Fig. 5d). Interestingly, all the samples showed excellent dehydrogenation activity of 12H-NEC, with the conversion rate of 12H-NEC close to 100 % and hydrogen release of about 5.5 wt%. The above conclusions also prove that the high activity of Pd/Mg(OH)₂ catalyst is due to the strong alkalinity of Mg(OH)₂ nanosheets, which makes Pd species form Pd(OH)₂ uniformly dispersed on the surface of Mg(OH)₂ nanosheets. Moreover, this phenomenon still exists in catalysts prepared by Al₂O₃ supporters with different acidity and alkalinity. The catalytic dehydrogenation activity of catalyst prepared with alkaline Pd/Al₂O₃-Alkaline is also higher than that of Pd/Al₂O₃-Acidity (Fig. S20). Therefore, enhancing the basicity of the support may be a good way to facilitate the dehydrogenation of 12H-NEC on Pd-based catalysts.

3.4. Computational studies

The experimental results have shown that the magnesium hydroxide nanosheet supported Pd nanoclusters show excellent catalytic dehydrogenation activity for 12H-NEC to NEC. In order to further understand the mechanism of 12H-NEC dehydrogenation reaction on Pd-based catalysts, DFT calculations were performed to compare the binding energies of different reaction intermediates on the surface of Pd/Mg(OH)₂



Scheme 1. The reversible hydrogenation and dehydrogenation process of the NEC/12H-NEC for hydrogen storage.

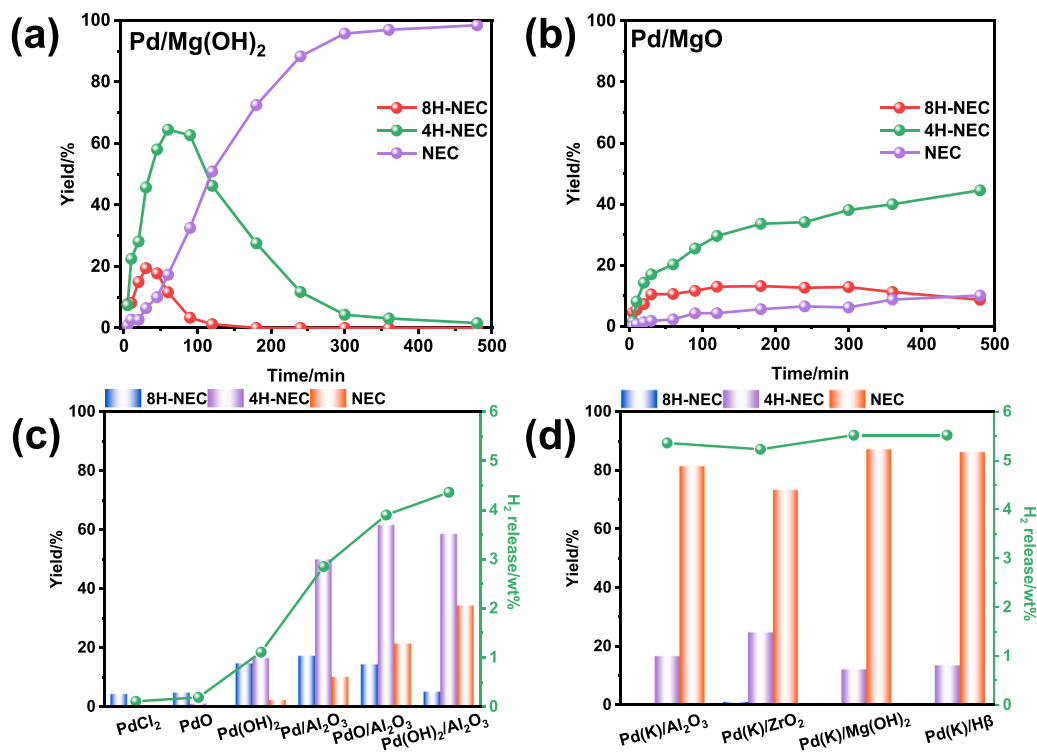


Fig. 5. Time-dependent product yield of for dehydrogenation of 12H-NEC over (a) Pd/Mg(OH)₂ and (b) Pd/MgO. Catalytic dehydrogenation performance of 12H-NEC over (c) different active metals and (d) Pd(K)/support catalysts. Reaction conditions: 5 g of 12H-LOHCs, 0.5 g of catalyst (2.5 mg Pd metal species), 180 °C of reaction temperature, and 6 h of reaction time.

and Pd/MgO catalysts. The optimized adsorption geometries and adsorption energies of 12H-NEC, 8H-NEC, 4H-NEC and NEC on Pd/Mg(OH)₂ and Pd/MgO surface are shown in Fig. 6, S21 and Table 2.

As the C-H bonds in 12H-NEC are saturated, the binding energy of 12H-NEC adsorbed on Pd-based catalyst is relatively low, which is

– 0.042 eV on Pd/MgO and – 0.058 eV on Pd/Mg(OH)₂, respectively. This result shows that the interaction between 12H-NEC and catalyst surface is weak, and Pd/Mg(OH)₂ is more favorable for the adsorption of 12H-NEC than Pd/MgO. Sotoodeh et al. showed that the dehydrogenation of 12H-NEC started from the C-H bonds adjacent to N heteroatom in

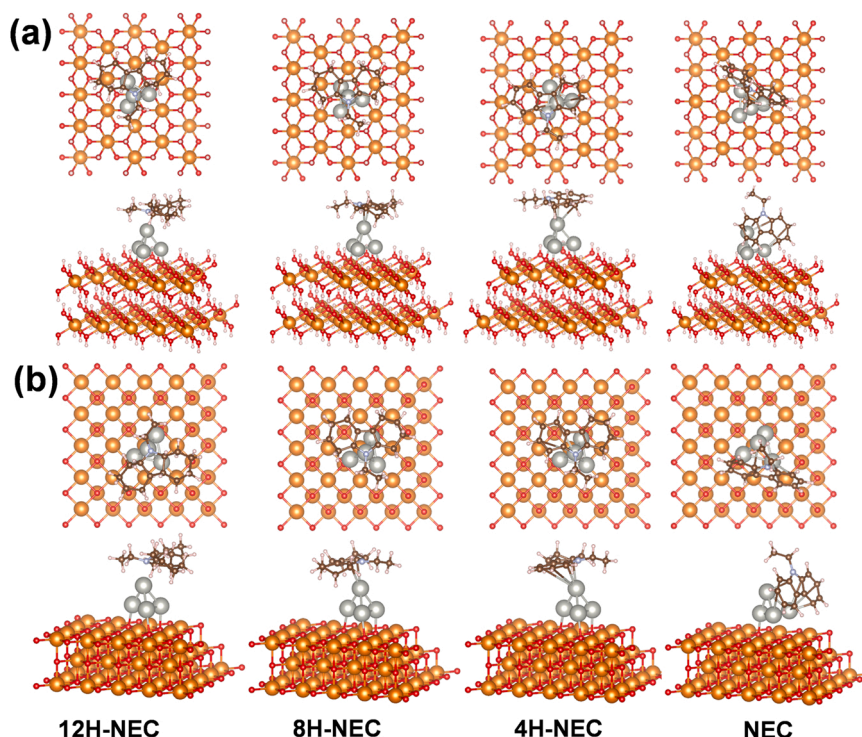


Fig. 6. Top and side views of the optimized adsorption geometries of 12H-NEC, 8H-NEC, 4H-NEC and NEC on the (a) Pd/Mg(OH)₂ and (b) Pd/MgO surfaces.

Table 2

DFT calculated adsorption energies of 12H-NEC, 8H-NEC, 4H-NEC and NEC on Pd/MgO and Pd/Mg(OH)₂ surfaces.

Samples	12H-NEC	8H-NEC	4H-NEC	NEC
Pd/MgO	-0.042	-0.042	-0.091	-0.139
Pd/Mg(OH) ₂	-0.058	-0.176	-0.528	-0.591

the five-membered ring, resulting in 8H-NEC [56]. After the optimization, 8H-NEC is adsorbed on Pd-based catalyst through C-Pd bonds, and the corresponding adsorption energies are -0.042 eV and -0.176 eV on Pd/MgO and Pd/Mg(OH)₂, respectively. It can be clearly seen that.

8H-NEC has strong interaction with Pd/Mg(OH)₂ surface. As for 4H-NEC, it is formed from 8H-NEC by removing the H atom in one of the six-membered rings [29]. The six-membered ring of 4H-NEC is adsorbed on catalysts surfaces C-Pd bonds. On the Pd/Mg(OH)₂ surface, the binding energy of 4H-NECZ was -0.528 eV, indicating that the catalyst prepared by Mg(OH)₂ nanosheets can significantly enhance the adsorption of 4H-NEC. Notably, the binding energy of NEC on the catalyst surface is much higher than that of 12H-NEC, 8H-NEC and 4H-NEC, which are -0.139 eV and -0.591 eV on Pd/MgO and Pd/Mg(OH)₂ respectively. The five-membered ring and two six-membered rings in NEC molecule are adsorbed on the catalyst surface. All in all, the results show that the binding energy of reactants and intermediates is increased on the surface of Pd/Mg(OH)₂, which indicates that magnesium hydroxide can promote the interaction between reaction intermediates and substrates.

The change of Gibbs free energies of 12H-NEC dehydrogenation to NEC on the Pd/Mg(OH)₂ and Pd/MgO surfaces were displayed in Table S3. It is found that the dehydrogenation barriers are higher than the adsorption energy by comparing the binding energy of reactants and intermediates on the catalyst surface and Gibbs free energy of dehydrogenation, which indicates that 12H-NEC, 8H-NEC and 4H-NEC tend to desorb on Pd/Mg(OH)₂ and Pd/MgO surfaces rather than dehydrogenate. Meanwhile, it also reveals that the dehydrogenation of 4H-NEC and the desorption of NEC compete with each other and affect the kinetic performance together. Besides, the energy profile of 12H-NEC dehydrogenation to NEC on the Pd/Mg(OH)₂ and Pd/MgO surfaces are shown in Fig. 7. It is clear that the dehydrogenation of 4H-NEC has the highest barrier in the whole dehydrogenation process, indicating that the dehydrogenation of 4H-NEC to NEC is the rate-limiting step, which is consistent with the experimental and reported results [30,57]. Compared with Pd/MgO, the barriers of the three dehydrogenation stages are lower on the surface of Pd/Mg(OH)₂, which indicates that Pd/Mg(OH)₂ shows higher catalytic activity and selectivity, which is consistent with the results of the dehydrogenation of 12H-NEC and kinetics analysis.

4. Conclusion

In summary, we successfully fabricated a Pd/Mg(OH)₂ catalyst with lower palladium loading (0.5 wt%) on the two-dimensional magnesium hydroxide nanosheets which exhibits excellent catalytic activity toward the dehydrogenations of 12H-NEC, 12H-NPC and 8H-MID, with highly efficient H₂ production. For the prepared Pd/Mg(OH)₂ catalyst, the conversion of 12H-NEC, the selectivity of NEC and the hydrogen release amount are 100 %, 97.12 % and 5.72 wt% respectively at 180 °C for 6 h, while those data over Pd/MgO catalyst are only 70.84 %, 7.65 % and 2.34 wt% at the same condition. The HAADF-STEM, XPS, EPR and EXAFS results show that Pd/Mg(OH)₂ catalyst has better metal dispersion and stronger metal support interaction. By exploring the dehydrogenation mechanism of 12H-NEC, it is found that the excellent catalytic activity of Pd/Mg(OH)₂ may be due to the strong alkalinity of magnesium hydroxide nanosheets promoting the formation of Pdⁿ⁺-OH structure. Besides, DFT calculations also revealed that the higher binding energy of reactants and intermediates and lower barriers of dehydrogenation reaction on the Pd/Mg(OH)₂ than Pd/MgO catalyst. Based

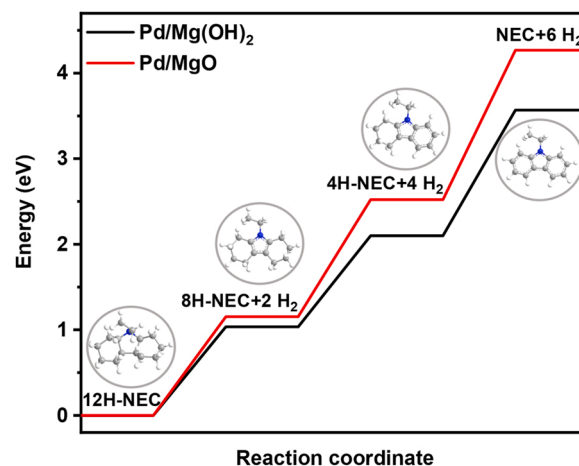


Fig. 7. DFT-calculated energy profile of 12H-NEC dehydrogenation to NEC on the Pd/Mg(OH)₂ and Pd/MgO surfaces.

on the above results, we believe that the high activity Pd-based catalyst using magnesium hydroxide nanosheets as support would be promising way for the dehydrogenation reactions, accelerate the developments and applications of hydrogen storage in LOHCs.

CRediT authorship contribution statement

Lixia Ge: Formal analysis, Experimental, Investigation, Writing – original draft. **Yanfeng Zhu:** Characterizations, Investigation. **Min-guang Qiu:** Investigation. **Shuai Yang:** EXAFS analysis. **Nannan Sun:** Supervision, Methodology. **Jiong Li:** EXAFS analysis. **Wei Wei:** Supervision. **Xinqing Chen:** Supervision, Methodology, Funding acquisition, Writing – review & editing.

Declaration of Competing Interest

The authors declare that they have no known competing financial interests or personal relationships that could have appeared to influence the work reported in this paper.

Data Availability

Data will be made available on request.

Acknowledgements

The authors acknowledge supports from National Natural Science Foundation of China (22078354) and National Key Research and Development Program of China (2022YFE0208300).

Supporting Information

Additional characterization of XRD patterns, SEM images, TEM and EDS images, FT-IR, N₂ absorption/desorption isotherms, XPS spectra and EXAFS fitting results; Catalytic dehydrogenation results of 12H-NEC, DFT-calculated results and references.

Appendix A. Supporting information

Supplementary data associated with this article can be found in the online version at [doi:10.1016/j.apcatb.2023.122793](https://doi.org/10.1016/j.apcatb.2023.122793).

References

- [1] Y.Q. Zou, N. von Wolff, A. Anaby, Y. Xie, D. Milstein, Ethylene glycol as an efficient and reversible liquid organic hydrogen carrier, *Nat. Catal.* 2 (2019) 415–422.

- [2] T. He, P. Pachfule, H. Wu, Q. Xu, P. Chen, Hydrogen carriers, *Nat. Rev. Mater.* 1 (2016) 16059.
- [3] Y. Guo, M. Wang, Q. Zhu, D. Xiao, D. Ma, Ensemble effect for single-atom, small cluster and nanoparticle catalysts, *Nat. Cat.* 5 (2022) 766–776.
- [4] J. Graetz, New approaches to hydrogen storage, *Chem. Soc. Rev.* 38 (2009) 73–82.
- [5] L. Ge, M. Qiu, Y. Zhu, S. Yang, W. Li, W. Li, Z. Jiang, X. Chen, Synergistic catalysis of Ru single-atoms and zeolite boosts high-efficiency hydrogen storage, *Appl. Catal. B-Environ.* 319 (2022), 121958.
- [6] A.F. Dalebrook, W. Gan, M. Grasmann, S. Moret, G. Laurenczy, Hydrogen storage: beyond conventional methods, *Chem. Commun.* 49 (2013) 8735–8751.
- [7] G. Sievi, D. Geburtig, T. Skeledzic, A. Bösmann, P. Preuster, O. Brummel, F. Waidhas, M.A. Montero, P. Khanipour, I. Katsounaros, J. Libuda, K.J. J. Mayrhofer, P. Wasserscheid, Towards an efficient liquid organic hydrogen carrier fuel cell concept, *Energy Environ. Sci.* 12 (2019) 2305–2314.
- [8] D. Teichmann, W. Arlt, P. Wasserscheid, R. Freymann, A future energy supply based on Liquid Organic Hydrogen Carriers (LOHC), *Energy Environ. Sci.* 4 (2011) 2767–2773.
- [9] E. Gianotti, M. Taillades-Jacquín, J. Rozière, D.J. Jones, High-purity hydrogen generation via dehydrogenation of organic carriers: a review on the catalytic process, *ACS Catal.* 8 (2018) 4660–4680.
- [10] Q.-L. Zhu, Q. Xu, Liquid organic and inorganic chemical hydrides for high-capacity hydrogen storage, *Energy Environ. Sci.* 8 (2015) 478–512.
- [11] H. Yu, X. Yang, X. Jiang, Y. Wu, S. Chen, W. Lin, Y. Wu, L. Xie, X. Li, J. Zheng, $\text{LaNi}_{5.5}$ particles for reversible hydrogen storage in N-ethylcarbazole, *Nano Energy* 80 (2021), 105476.
- [12] B. Wang, T.-y Chang, Z. Jiang, J.-j Wei, T. Fang, Component controlled synthesis of bimetallic PdCu nanoparticles supported on reduced graphene oxide for dehydrogenation of dodecahydro-N-ethylcarbazole, *Appl. Catal. B-Environ.* 251 (2019) 261–272.
- [13] D. Forberg, T. Schwob, M. Zaheer, M. Friedrich, N. Miyajima, R. Kempe, Single-catalyst high-weight % hydrogen storage in an N-heterocycle synthesized from lignin hydrogenolysis products and ammonia, *Nat. Commun.* 7 (2016) 13201.
- [14] L. Zhou, L. Sun, L. Xu, C. Wan, Y. An, M. Ye, Recent developments of effective catalysts for hydrogen storage technology using N-ethylcarbazole, *Catalysts* 10 (2020) 648.
- [15] L. Wang, J. Diao, M. Peng, Y. Chen, X. Cai, Y. Deng, F. Huang, X. Qin, D. Xiao, Z. Jiang, N. Wang, T. Sun, X. Wen, H. Liu, D. Ma, Cooperative sites in fully exposed Pd clusters for low-temperature direct dehydrogenation reaction, *ACS Catal.* 11 (2021) 11469–11477.
- [16] A. Zhang, J. Xia, Q. Yao, Z.-H. Lu, Pd-WOx heterostructures immobilized by MOFs-derived carbon cage for formic acid dehydrogenation, *Appl. Catal. B-Environ.* 309 (2022), 121278.
- [17] M. Amende, C. Gleichweit, K. Werner, S. Schernich, W. Zhao, M.P. Lorenz, O. Hofert, C. Papp, M. Koch, P. Wasserscheid, M. Laurin, H.P. Steinruck, J. Libuda, Model catalytic studies of liquid organic hydrogen carriers: dehydrogenation and decomposition mechanisms of dodecahydro-N-ethylcarbazole on Pt(111), *ACS Catal.* 4 (2014) 657–665.
- [18] X. Chen, M. Peng, X. Cai, Y. Chen, Z. Jia, Y. Deng, B. Mei, Z. Jiang, D. Xiao, X. Wen, N. Wang, H. Liu, D. Ma, Regulating coordination number in atomically dispersed Pt species on defect-rich graphene for n-butane dehydrogenation reaction, *Nat. Commun.* 12 (2021) 2664.
- [19] Z. Jia, X. Qin, Y. Chen, X. Cai, Z. Gao, M. Peng, F. Huang, D. Xiao, X. Wen, N. Wang, Z. Jiang, W. Zhou, H. Liu, D. Ma, Fully-exposed Pt-Fe cluster for efficient preferential oxidation of CO towards hydrogen purification, *Nat. Commun.* 13 (2022) 6798.
- [20] J. Zhang, Y. Deng, X. Cai, Y. Chen, M. Peng, Z. Jia, Z. Jiang, P. Ren, S. Yao, J. Xie, D. Xiao, X. Wen, N. Wang, H. Liu, D. Ma, Tin-assisted fully exposed platinum clusters stabilized on defect-rich graphene for dehydrogenation reaction, *ACS Catal.* 9 (2019) 5998–6005.
- [21] W. Xue, H. Liu, B. Mao, H. Liu, M. Qiu, C. Yang, X. Chen, Y. Sun, Reversible hydrogenation and dehydrogenation of N-ethylcarbazole over bimetallic Pd-Rh catalyst for hydrogen storage, *Chem. Eng. J.* 421 (2021), 127781.
- [22] F. Sotoodeh, B.J.M. Huber, K.J. Smith, Dehydrogenation kinetics and catalysis of organic heteroaromatics for hydrogen storage, *Int. J. Hydrogen Energy* 37 (2012) 2715–2722.
- [23] Z. Jiang, X. Gong, B. Wang, Z. Wu, T. Fang, A experimental study on the dehydrogenation performance of dodecahydro-N-ethylcarbazole on M/TiO_2 catalysts, *Int. J. Hydrogen Energy* 44 (2019) 2951–2959.
- [24] F. Sotoodeh, K.J. Smith, Analysis of H_2 release from organic polycyclics over Pd catalysts using DFT, *J. Phys. Chem. C* 117 (2012) 194–204.
- [25] M. Amende, S. Schernich, M. Sobota, I. Nikiforidis, W. Hieringer, D. Assenbaum, C. Gleichweit, H.J. Drescher, C. Papp, H.P. Steinruck, A. Gorling, P. Wasserscheid, M. Laurin, J. Libuda, Dehydrogenation mechanism of liquid organic hydrogen carriers: dodecahydro-N-ethylcarbazole on Pd(111), *Chem* 19 (2013) 10854–10865.
- [26] P. Wang, S. Fan, X. Li, J. Wang, Z. Liu, Z. Niu, M.O. Tadé, S. Liu, Single Pd atoms synergistically manipulating charge polarization and active sites for simultaneously photocatalytic hydrogen production and oxidation of benzylamine, *Nano Energy* 95 (2022), 107045.
- [27] J. Zhang, M. Wang, Z. Gao, X. Qin, Y. Xu, Z. Wang, W. Zhou, D. Ma, Importance of species heterogeneity in supported metal catalysts, *J. Am. Chem. Soc.* 144 (2022) 5108–5115.
- [28] Y. Deng, Y. Guo, Z. Jia, J.C. Liu, J. Guo, X. Cai, C. Dong, M. Wang, C. Li, J. Diao, Z. Jiang, J. Xie, N. Wang, H. Xiao, B. Xu, H. Zhang, H. Liu, J. Li, D. Ma, Few-atom Pt ensembles enable efficient catalytic cyclohexane dehydrogenation for hydrogen production, *J. Am. Chem. Soc.* 144 (2022) 3535–3542.
- [29] M. Yang, Y. Dong, S. Fei, H. Ke, H. Cheng, A comparative study of catalytic dehydrogenation of perhydro-N-ethylcarbazole over noble metal catalysts, *Int. J. Hydrogen Energy* 39 (2014) 18976–18983.
- [30] C. Dong, Z. Gao, Y. Li, M. Peng, M. Wang, Y. Xu, C. Li, M. Xu, Y. Deng, X. Qin, F. Huang, X. Wei, Y.-G. Wang, H. Liu, W. Zhou, D. Ma, Fully exposed palladium cluster catalysts enable hydrogen production from nitrogen heterocycles, *Nat. Catal.* 5 (2022) 485–493.
- [31] H. Chen, H. Shuang, W. Lin, X. Li, Z. Zhang, J. Li, J. Fu, Tuning interfacial electronic properties of palladium oxide on vacancy-abundant carbon nitride for low-temperature dehydrogenation, *ACS Catal.* 11 (2021) 6193–6199.
- [32] H. Shuang, H. Chen, F. Wu, J. Li, C. Cheng, H. Li, J. Fu, Catalytic dehydrogenation of hydrogen-rich liquid organic hydrogen carriers by palladium oxide supported on activated carbon, *Fuel* 275 (2020), 117896.
- [33] Y.-X. Tuo, L.-J. Shi, H.-Y. Cheng, Y.-A. Zhu, M.-L. Yang, J. Xu, Y.-F. Han, P. Li, W.-K. Yuan, Insight into the support effect on the particle size effect of Pt/C catalysts in dehydrogenation, *J. Catal.* 360 (2018) 175–186.
- [34] J. Oh, T.W. Kim, K. Jeong, J.H. Park, Y.-W. Suh, Enhanced activity and stability of a carbon-coated alumina-supported Pd Catalyst in the dehydrogenation of a liquid organic hydrogen carrier, perhydro 2-(n-methylbenzyl)pyridine, *ChemCatChem* 10 (2018) 3892–3900.
- [35] X. Lin, J. Zhou, Y. Fan, Y. Zhan, C. Chen, D. Li, L. Jiang, Mg-Al hydrotalcite-supported Pd catalyst for low-temperature CO oxidation: effect of $\text{Pd}^{(II)}$ species and surface hydroxyl groups, *Dalton Trans.* 47 (2018) 14938–14944.
- [36] M. Chu, J. Huang, J. Gong, Y. Qu, G. Chen, H. Yang, X. Wang, Q. Zhong, C. Deng, M. Cao, J. Chen, X. Yuan, Q. Zhang, Synergistic combination of Pd nanosheets and porous $\text{Bi}(\text{OH})_3$ boosts activity and durability for ethanol oxidation reaction, *Nano Res.* 15 (2022) 3920–3926.
- [37] H. Yang, M. Luo, S. Lu, Q. Zhang, Y. Chao, F. Lv, L. Zhu, L. Bai, L. Yang, W. Wang, D. Wei, Y. Liang, L. Gu, H. Chen, S. Guo, Low-temperature aerobic oxidation of thiophenic sulfides over atomic Mo hosted by cobalt hydroxide sub-nanometer sheets, *Chem* 8 (2022) 2460–2471.
- [38] T. Ishida, R. Tsunoda, Z. Zhang, A. Hamasaki, T. Honma, H. Ohashi, T. Yokoyama, M. Tokunaga, Supported palladium hydroxide-catalyzed intramolecular double C-H bond functionalization for synthesis of carbazoles and dibenzofurans, *Appl. Catal. B-Environ.* 150–151 (2014) 523–531.
- [39] G. Kresse, J. Furthmüller, Efficiency of ab-initio total energy calculations for metals and semiconductors using a plane-wave basis set, *Comp. Mater. Sci.* 6 (1996) 15–50.
- [40] G. Kresse, J. Furthmüller, Efficient iterative schemes for ab initio total-energy calculations using a plane-wave basis set, *Phys. Rev. B* 54 (1996) 11169–11186.
- [41] J.P. Perdew, K. Burke, M. Ernzerhof, Generalized gradient approximation made simple, *Phys. Rev. Lett.* 77 (1996) 3865–3868.
- [42] P.E. Blöchl, Projector augmented-wave method, *Phys. Rev. B* 50 (1994) 17953–17979.
- [43] J.M. Hanlon, L. Bravo Diaz, G. Balducci, B.A. Stobbs, M. Bielewski, P. Chung, I. MacLaren, D.H. Gregory, Rapid surfactant-free synthesis of $\text{Mg}(\text{OH})_2$ nanoplates and pseudomorphic dehydration to MgO , *CryptComm* 17 (2015) 5672–5679.
- [44] P. Liu, P.M. Abdala, G. Goubert, M.G. Willinger, C. Cooper, Ultrathin single crystalline $\text{MgO}(111)$ Nanosheets*, *Angew. Chem. Int. Ed. Engl.* 60 (2021) 3254–3260.
- [45] A.M. Haggag, A.E. Awadallah, A.A. Aboul-Enein, G.H. Sayed, Non-oxidative conversion of real low density polyethylene waste into hydrogen and carbon nanomaterials over MgO supported bimetallic Co-Mo catalysts with different total Co-Mo contents, *Chem. Eng. Sci.* 247 (2022), 117092.
- [46] T.W. Kim, S.H. Ko, M. Kim, Y.-W. Suh, Efficient hydrogen charge into monobenzyltoluene over Ru/MgO catalysts synthesized by thermolysis of $\text{Ru}_3(\text{CO})_{12}$ on porous $\text{Mg}(\text{OH})_2$ powder, *Adv. Powder Technol.* 31 (2020) 1682–1692.
- [47] L. Yang, Z. Pan, D. Wang, S. Wang, X. Wang, H. Ma, H. Liu, C. Wang, W. Qu, Z. Tian, Highly effective $\text{Pd}/\text{MgO}/\gamma\text{-Al}_2\text{O}_3$ catalysts for CO oxidative coupling to dimethyl oxalate: the effect of MgO coating on $\gamma\text{-Al}_2\text{O}_3$, *ACS Appl. Mater. Interfaces* 13 (2021) 28064–28071.
- [48] Z. Liu, J.A. Cortés-Concepción, M. Mustian, M.D. Amiridis, Effect of basic properties of MgO on the heterogeneous synthesis of flavanone, *Appl. Catal. A-Gen.* 302 (2006) 232–236.
- [49] O. Lupan, V. Postica, M. Hoppe, N. Wolff, O. Polonskyi, T. Pauporte, B. Viana, O. Majerus, L. Kienle, F. Faupel, R. Adelung, PdO/PdO_2 functionalized ZnO : Pd films for lower operating temperature H_2 gas sensing, *Nanoscale* 10 (2018) 14107–14127.
- [50] J. Li, Q. Guan, H. Wu, W. Liu, Y. Lin, Z. Sun, X. Ye, X. Zheng, H. Pan, J. Zhu, S. Chen, W. Zhang, S. Wei, J. Lu, Highly active and stable metal single-atom catalysts achieved by strong electronic metal-support interactions, *J. Am. Chem. Soc.* 141 (2019) 14515–14519.
- [51] P. Liu, Z. Huang, X. Gao, X. Hong, J. Zhu, G. Wang, Y. Wu, J. Zeng, X. Zheng, Synergy between palladium single atoms and nanoparticles via hydrogen spillover for enhancing CO_2 photoreduction to CH_4 , *Adv. Mater.* 34 (2022) 2200057.
- [52] X. Lu, C. Guo, M. Zhang, L. Leng, J.H. Horton, W. Wu, Z. Li, Rational design of palladium single-atoms and clusters supported on silicoaluminophosphate-31 by a photochemical route for chemoselective hydrodeoxygenation of vanillin, *Nano Res.* 14 (2021) 4347–4355.
- [53] A. Corma, P. Concepción, M. Boronat, M.J. Sabater, J. Navas, M.J. Yacaman, E. Larios, A. Posadas, M.A. López-Quintela, D. Buceta, E. Mendoza, G. Guilera, A. Mayoral, Exceptional oxidation activity with size-controlled supported gold clusters of low atomicity, *Nat. Chem.* 5 (2013) 775–781.

- [54] C. Dong, Y. Li, D. Cheng, M. Zhang, J. Liu, Y.-G. Wang, D. Xiao, D. Ma, Supported metal clusters: fabrication and application in heterogeneous catalysis, *ACS Catal.* 10 (2020) 11011–11045.
- [55] T.W. Kim, M. Kim, S.K. Kim, Y.N. Choi, M. Jung, H. Oh, Y.-W. Suh, Remarkably fast low-temperature hydrogen storage into aromatic benzyltoluenes over MgO-supported Ru nanoparticles with homolytic and heterolytic H₂ adsorption, *Appl. Catal. B-Environ.* 286 (2021), 119889.
- [56] F. Sotoodeh, K.J. Smith, Structure sensitivity of dodecahydro-N-ethylcarbazole dehydrogenation over Pd catalysts, *J. Catal.* 279 (2011) 36–47.
- [57] S. Kiermaier, D. Lehmann, A. Bösmann, P. Wasserscheid, Dehydrogenation of perhydro-N-ethylcarbazole under reduced total pressure, *Int. J. Hydrogen Energy* 46 (2021) 15660–15670.